

3D Relativistic Magnetohydrodynamic Simulations of Current-Driven Instability. I. Instability of a static column

Yosuke Mizuno^{1,2}, Yuri Lyubarsky³, Ken-Ichi Nishikawa^{1,2}, and Philip E. Hardee⁴

ABSTRACT

We have investigated the development of current-driven (CD) kink instability through three-dimensional relativistic MHD simulations. A static force-free equilibrium helical magnetic configuration is considered in order to study the influence of the initial configuration on the linear and nonlinear evolution of the instability. We found that the initial configuration is strongly distorted but not disrupted by the kink instability. The instability develops as predicted by linear theory. In the non-linear regime the kink amplitude continues to increase up to the terminal simulation time, albeit at different rates, for all but one simulation. The growth rate and nonlinear evolution of the CD kink instability depends moderately on the density profile and strongly on the magnetic pitch profile. The growth rate of the kink mode is reduced in the linear regime by an increase in the magnetic pitch with radius and the non-linear regime is reached at a later time than for constant helical pitch. On the other hand, the growth rate of the kink mode is increased in the linear regime by a decrease in the magnetic pitch with radius and reaches the non-linear regime sooner than the case with constant magnetic pitch. Kink amplitude growth in the non-linear regime for decreasing magnetic pitch leads to a slender helically twisted column wrapped by magnetic field. On the other hand, kink amplitude growth in the non-linear regime nearly ceases for increasing magnetic pitch.

Subject headings: instabilities - MHD - methods: numerical - galaxies: jets

1. Introduction

Relativistic jets occur in active galactic nuclei (**AGN**) (e.g., Urry & Padovani 1995; Ferrari 1998; Meier et al. 2001), occur in microquasars (e.g., Mirabel & Rodriguez 1999), and are thought responsible for the gamma-ray bursts (**GRB**) (e.g., Zhang & Mészáros 2004; Piran 2005; Mészáros

¹Center for Space Plasma and Aeronomic Research, University of Alabama in Huntsville ,320 Sparkman Drive, NSSTC, Huntsville, AL 35805, USA; mizuno@cspar.uah.edu

²National Space Science and Technology Center, V62, Huntsville, AL 35805, USA

³Physics Department, Ben-Gurion University, Beer-Sheva 84105, Israel

⁴Department of Physics and Astronomy, The University of Alabama, Tuscaloosa, AL 35487, USA

2006). The most promising mechanism for producing relativistic jets involves magnetohydrodynamic acceleration from an accretion disk around a black hole (e.g., Blandford 1976; Lovelace 1976; Blandford & Payne 1982; Fukue 1990; Meier 2005; Narayan et al. 2007), and/or involves the extraction of energy from a rotating black hole (Penrose 1969; Blandford & Znajek 1977).

General relativistic magnetohydrodynamic (**GRMHD**) codes have been used to study the extraction of rotational energy from a spinning black hole, i.e., Blandford-Znajek mechanism (Koide 2003; Komissarov 2005; McKinney 2005; Komissarov & McKinney 2007; Komissarov & Barkov 2009) and from an accretion disk, i.e., Blandford-Payne mechanism (Blandford & Payne 1982). GRMHD codes also probe the formation of GRB jets in collapsars (e.g., Mizuno et al. 2004a, 2004b; Liu et al. 2007; Barkov & Komissarov 2008; Stephens et al. 2008; Nagataki 2009; Komissarov & Barkov 2009) and are used to study the propagation of jets injected from an unresolved Keplerian disk (e.g., Komissarov et al. 2007, 2008; Tchekhovskoy et al. 2008, 2009). GRMHD simulations with a spinning black hole indicate jet production with a magnetically dominated high Lorentz factor spine with $v \sim c$, and a matter dominated sheath with $v \gtrsim c/2$ possibly embedded in a lower speed, $v \ll c$, disk/coronal wind (e.g., De Villiers et al. 2003, 2005; Hawley & Krolik 2006; McKinney & Gammie 2004; McKinney 2006; McKinney & Narayan 2007a, 2007b; McKinney & Brandford 2008; Beckwith et al. 2008; Hardee et al. 2007). Circumstantial evidence such as the requirement for large Lorentz factors suggested by the TeV BL Lacs when contrasted with much slower observed motions (Ghisellini et al. 2005) suggests such a spine-sheath morphology, although alternative interpretations are also possible (Georganopoulos & Kazanas 2003; Bromberg & Levinson 2008; Stern & Poutanen 2008; Giannios et al. 2009).

Numerical simulations indicate that the jet spine and sheath are accelerated and, in part, collimated by strong magnetic fields twisted in the rotating black hole ergosphere and in the accretion disk, respectively. The helically twisted magnetic fields are expected to be dominated by the toroidal component in the far zone as a result of jet expansion because the poloidal component falls off faster with expansion and distance. In configurations with strong toroidal magnetic field the current driven (**CD**) kink mode is unstable. This instability excites large-scale helical motions that can strongly distort or even disrupt the system. For static cylindrical force-free equilibria, the well-known Kruskal-Shafranov criterion states that the instability develops if the length of the column, ℓ , is long enough for the field lines to go around the cylinder at least once (e.g. Bateman 1978): $|B_p/B_\phi| < \ell/2\pi R$. This criterion suggests that jets are unstable beyond the Alfvén surface because of $B_p \lesssim B_\phi$ and $\ell \gtrsim R_j$ at the Alfvén surface, where R_j is the cylindrical radius of the jet. However, rotation and shear motions could significantly affect the instability criterion. For relativistic force-free configurations, the linear instability criteria were studied by Istomin & Pariev (1994, 1996), Begelman (1998), Lyubarskii (1999), Tomimatsu et al. (2001) and Narayan et al. (2009).

The linear mode analysis provides conditions for the instability but says little about the impact the instability has on the system. The instability of the potentially disruptive kink mode found from a linear analysis must be followed into the non-linear regime. The nonlinear development

of the CD kink instability is different for external and internal kink modes (e.g., Bateman 1978). External disruptive instability develops in a current carrying plasma column surrounded by a vacuum magnetic field. In astrophysical systems, some amount of plasma is present everywhere. In this case an internal kink instability develops inside a resonant surface on which the helicity of the magnetic field lines matches that of the eigenmode. In dissipationless MHD, the internal instability is known to saturate. Finite resistivity makes the internal kink mode disruptive but the time-scale significantly exceeds the Alfvén time-scale and may be too long to disrupt a fast outflow. In this case helical structures may be formed in the flow. Recently helical structures have been found in non-relativistic/relativistic simulations of magnetized jets (e.g., Lery et al. 2000; Ouyed et al. 2003; Nakamura & Meier 2004; Nakamura et al. 2007; Moll et al. 2008; McKinney & Blandford 2008; Carey & Sovinec 2009).

Twisted structures are observed in many AGN jets on sub-parsec, parsec and kiloparsec scales (e.g., Gómez et al. 2001; Lobanov & Zensus 2001). Dissipation processes may result in relaxation to helical equilibrium as evoked by Königl & Choudhuri (1985) for helical structures in AGN jets. In the absence of CD kink instability and resistive relaxation, helical structures may be attributed to the Kelvin-Helmholtz (**KH**) helical instability driven by velocity shear at the boundary between the jet and the surrounding medium (e.g., Hardee 2004, 2007) or triggered by precession of the jet ejection axis (Begelman et al. 1980). It is still not clear whether current driven, velocity shear driven or jet precession is responsible for the observed structures, or whether these different processes are responsible for the observed twisted structures at different spatial scales.

This is the first in a series of papers in which we study kink instability in relativistic systems. By relativistic we mean not only relativistically moving systems but any with magnetic energy density comparable to or greater than the plasma energy density, including the rest mass energy. In this paper, we present 3D results of the CD kink instability of a static plasma column. We start from static configurations because in the case of interest, the source of the free energy is the magnetic field, not the kinetic energy. Therefore static configurations (or more generally rigidly moving flows considered in the proper reference frame) are the simplest ones for studying the basic properties of the kink instability. At the next stage, we will investigate the influence of shear motions and rotation on the stability and nonlinear behavior of jets. This article is organized as follows. We describe the numerical method and setup used for our simulations in §2, present our results in §3, discuss the astrophysical implications in §4, and present some numerical tests in the Appendix.

2. Numerical Method

In order to study time evolution of the CD kink instability in the relativistic MHD (**RMHD**) regime, we use the 3D GRMHD code “RAISHIN” in Cartesian coordinates. RAISHIN is based on a $3 + 1$ formalism of the general relativistic conservation laws of particle number and energy momentum, Maxwell’s equations, and Ohm’s law with no electrical resistance (ideal MHD con-

dition) in a curved spacetime (Mizuno et al. 2006). In the RAISHIN code, a conservative, high-resolution shock-capturing scheme is employed. The numerical fluxes are calculated using the HLL approximate Riemann solver, and flux-interpolated, constrained transport is used to maintain a divergence-free magnetic field. The RAISHIN code has proven to be accurate to second order and has passed a number of numerical tests including highly relativistic cases and highly magnetized cases in both special and general relativity (Mizuno et al. 2006). The RAISHIN code performs special relativistic calculations in Minkowski spacetime by changing the metric.

For our simulations we will choose a force-free helical magnetic field as the initial configuration. A force-free configuration is a reasonable choice for the strong magnetic field cases that we study here. In general, the force-free equilibrium of a static cylinder is described by the equation

$$B_z \frac{dB_z}{dR} + \frac{B_\phi}{R} \frac{dB_\phi}{dR} = 0. \quad (1)$$

In particular we choose a poloidal magnetic field component of the form

$$B_z = \frac{B_0}{[1 + (R/a)^2]^\alpha}, \quad (2)$$

for which one finds a toroidal magnetic field component of the form

$$B_\phi = \frac{B_0}{(R/a)[1 + (R/a)^2]^\alpha} \sqrt{\frac{[1 + (R/a)^2]^{2\alpha} - 1 - 2\alpha(R/a)^2}{2\alpha - 1}}, \quad (3)$$

where R is the cylindrical radial position normalized by a simulation scale unit $L \equiv 1$, B_0 parameterizes the magnetic field amplitude, a is the characteristic radius of the column, and α is the pitch profile parameter. The pitch profile parameter determines the radial profile of the magnetic pitch $P = RB_z/B_\phi$, and provides a measure of the twist of the magnetic field lines. With our choice for the force-free field, the magnetic pitch can be written as

$$P = (R/a)^2 \sqrt{\frac{2\alpha - 1}{[1 + (R/a)^2]^{2\alpha} - 1 - 2\alpha(R/a)^2}}. \quad (4)$$

If the pitch profile parameter $\alpha < 1$, the magnetic pitch increases with radius. If $\alpha > 1$, the magnetic pitch decreases. When $\alpha = 1$, the magnetic pitch is constant. This configuration is the same as that used in previous non-relativistic work (Appl et al. 2000; Baty 2005).

The simulation grid is periodic along the axial direction. As a consequence the allowed axial wavelengths are restricted to $\lambda = L_z/n \leq L_z$, with n a positive integer and L_z is the grid length. The grid is a Cartesian (x, y, z) box of size $4L \times 4L \times L_z$ with grid resolution of $\Delta L = L/40$. In simulations we choose two different column radii, a , relative to the column length, L_z : (case A) $a = (1/16)L_z = (1/8)L$ and (case B) $a = (1/12)L_z = (1/4)L$. For case A $L_z = 2L$ and for case B $L_z = 3L$. In terms of a , the simulation box size is $32a \times 32a \times 16a$ for case A and $16a \times 16a \times 12a$ for case B. We impose outflow boundary conditions on the transverse boundaries at $x = y = \pm 2L$ ($x = y = \pm 16a$ for case A and $x = y = \pm 8a$ for case B).

We consider a low gas pressure medium with constant $p = p_0 = 0.02\rho_0 c^2$ for the equilibrium state, and two different density profiles: (case u) uniform density $\rho = 1.0\rho_0$ and (case n) non-uniform density decreasing proportional to the magnetic field strength, $\rho = \rho_1 B^2$ with $\rho_1 = 10.0\rho_0$. The equation of state is that of an ideal gas with $p = (\Gamma - 1)\rho e$, where e is the specific internal energy density and the adiabatic index $\Gamma = 5/3$. The specific enthalpy is $h \equiv 1 + e/c^2 + p/\rho c^2$. The magnetic field amplitude is $B_0 = 0.4\sqrt{4\pi\rho_0 c^2}$ leading to a low plasma- β near the axis. The sound speed is $c_s = (\Gamma p/\rho h)^{1/2}$ and the Alfvén speed is $v_A = [B^2/(\rho h + B^2)]^{1/2}$.

In order to investigate different radial pitch profiles, we perform simulations with: (case 1) constant pitch, $\alpha = 1$, (case 2) increasing pitch, $\alpha = 0.75$, and (case 3) decreasing pitch $\alpha = 2.0$. The radial profiles of the magnetic field components, the magnetic pitch, and the sound and Alfvén speeds for the different cases are shown in Figure 1. The radial profile of the magnetic field components for cases A and B are the same when normalized by a .

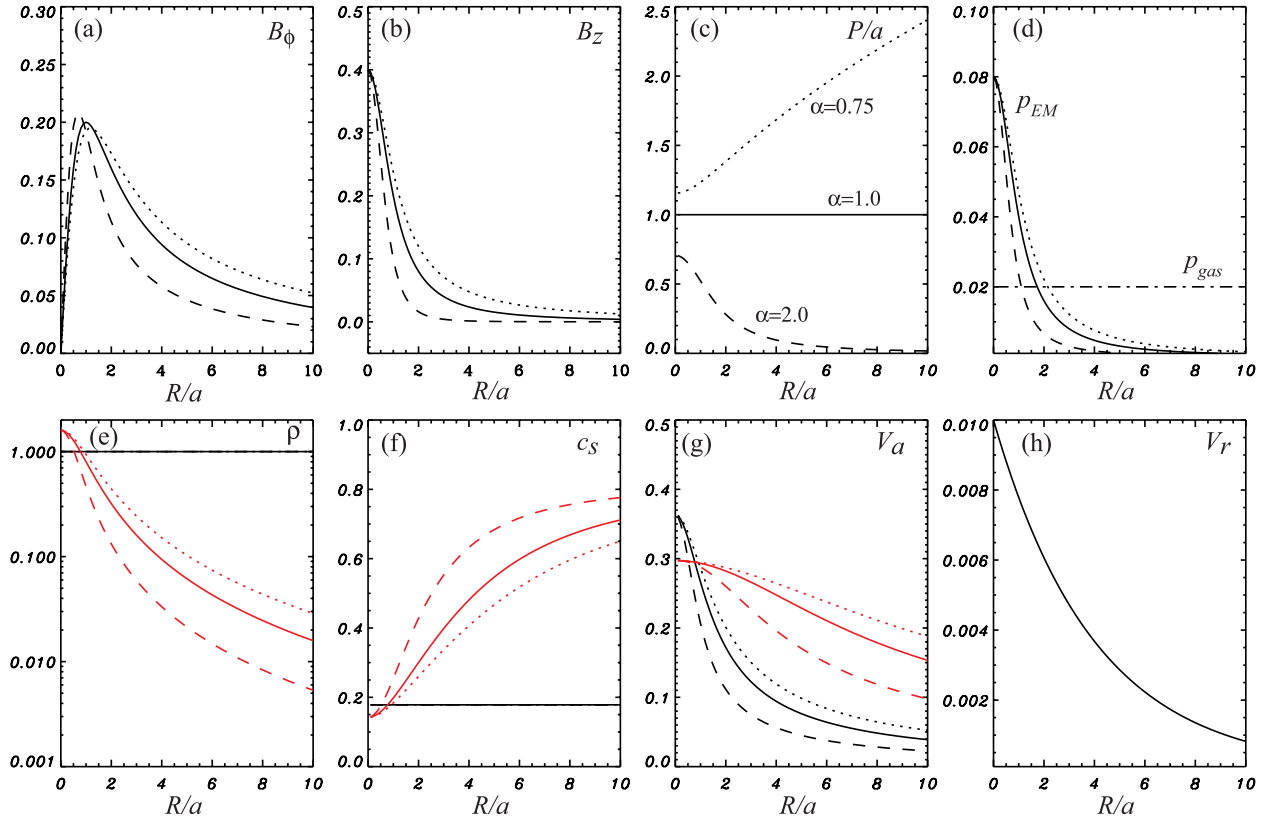


Fig. 1.— Radial profile of (a) the toroidal magnetic field (B_ϕ), (b) the axial magnetic field (B_z), (c) the magnetic pitch, $P = RB_z/B_\phi$, (d) magnetic and gas (dash-dot line) pressure, (e) the rest mass density, (f) the sound speed, and (g) the Alfvén speed. Uniform density cases are in black and declining density cases are in red where (solid) indicates constant pitch, (dotted) indicates increasing pitch, and (dashed) indicates decreasing pitch. The radial velocity perturbation profile is shown in panel (h).

The initial MHD equilibrium configuration is perturbed by a small radial velocity with profile given by

$$v_R = \delta v \exp\left(-\frac{R}{R_a}\right) \cos(m\theta) \sin\left(\frac{2\pi n z}{L_z}\right). \quad (5)$$

The amplitude of the perturbation is taken to be $\delta v = 0.01c$ with radial width $R_a = 0.5L$ ($4a$ for case A and $2a$ for case B). We choose $m = 1$ and $n = 1$ in the above formula. This is identical to imposing $(m, n) = (-1, -1)$, because of the symmetry between (m, n) and $(-m, -n)$ pairs. The various different cases that we have considered are listed in Table 1.

Table 1. Models and Parameters

Case	a/L	α	ρ	Pitch	L_z/L	L_z/a	v_{A0}/c
A1u	0.125	1.0	uniform	constant	2.0	16	0.4
A1n	0.125	1.0	decrease	constant	2.0	16	0.3
B1u	0.25	1.0	uniform	constant	3.0	12	0.4
B1n	0.25	1.0	decrease	constant	3.0	12	0.3
A2u	0.125	0.75	uniform	increase	2.0	16	0.4
A3u	0.125	2.0	uniform	decrease	2.0	16	0.4
B2u	0.25	0.75	uniform	increase	3.0	12	0.4
B3u	0.25	2.0	uniform	decrease	3.0	12	0.4
A2n	0.125	0.75	decrease	increase	2.0	16	0.3
A3n	0.125	2.0	decrease	decrease	2.0	16	0.3
B2n	0.25	0.75	decrease	increase	3.0	12	0.3
B3n	0.25	2.0	decrease	decrease	3.0	12	0.3

3. Results

3.1. Time evolution of the CD kink instability

As an indicator of the growth of the CD kink instability we use the volume-averaged kinetic energy transverse to the z -axis within a cylinder of radius $R/L \leq 1.0$ written as

$$E_{kin,xy} = \frac{1}{V_b} \int_{V_b} \frac{\rho v_x^2 + \rho v_y^2}{2} dx dy dz \quad (6)$$

and normalized by the initial volume-averaged transverse magnetic energy. The quantity $E_{kin,xy}$ allows determination of different evolutionary stages (initial exponential (linear growth phase) growth, and subsequent non-linear evolution). In all cases, the initial growth regime is characterized by an exponential increase in $E_{kin,xy}$ by several orders of magnitude to a maximum amplitude followed by a slow decline in the non-linear regime. The time evolution of the maximum radial velocity evaluated over half the grid length, $L_z/2$, shows a growth trend similar to the growth of $E_{kin,xy}$.

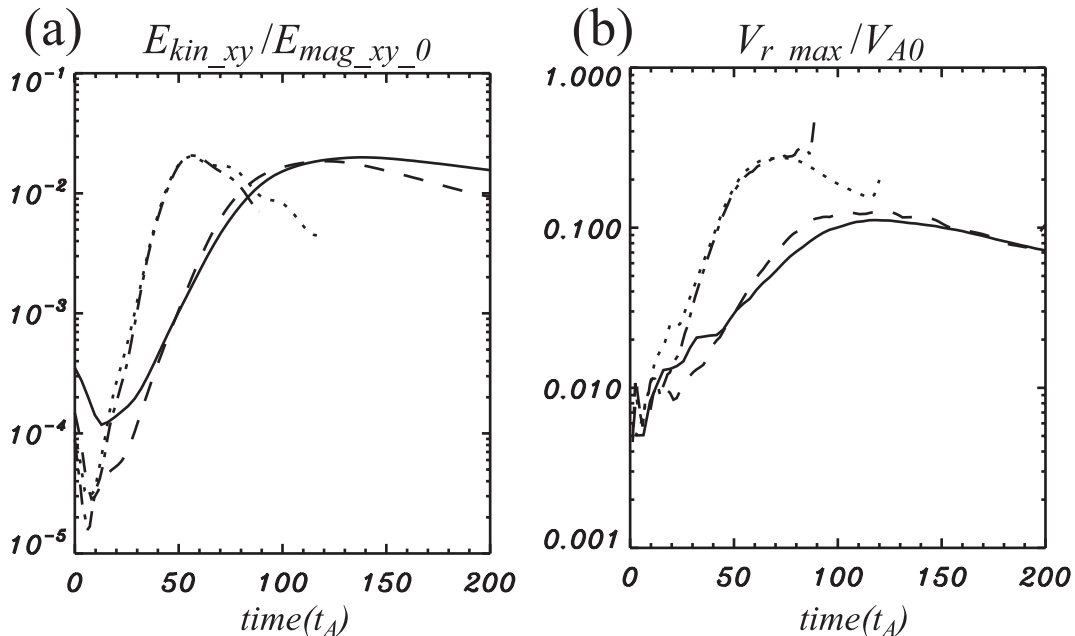


Fig. 2.— Time evolution of (a) $E_{kin,xy}$ within $R/L \leq 1.0$ normalized by the initial volume-averaged magnetic energy and (b) the maximum radial velocity normalized by the Alfvén velocity on the axis (v_{A0}) for constant pitch ($\alpha = 1.0$). Case A, $a = (1/16)L_z$: uniform density (solid line) and decreasing density (dotted line). Case B, $a = (1/12)L_z$: uniform density (dashed line) and decreasing density (dash-dotted line). Time is in units of $t_A = a/v_{A0}$, where v_{A0} is initial Alfvén velocity on the axis. Note that normalizing values of $E_{mag,xy,0}$, v_{A0} and the timescale units, t_A , are different for uniform and decreasing density cases.

Figure 2 shows the time evolution of $E_{kin,xy}$ and maximum radial velocity for cases A and B with constant pitch for uniform and decreasing radial density profiles. The effect of changing the characteristic radius, a , relative to the grid length, L_z , is equivalent to changing the wavelength. The wavelength in case A is $\lambda = 16 a$, and in case B is $\lambda = 12 a$. Note that according to the Kruskal-Shafranov criterion, the instability develops at $\lambda > 2\pi a$. The instability growth rate reaches a maximum at $\lambda_{max} \approx 10 a$, the exact coefficient being dependent on the transverse distribution of the density and magnetic pitch. Specifically in the case of constant pitch and uniform density, Appl et al. (2000) found $\lambda_{max} = 8.43 a$ and a corresponding growth rate of $\Gamma_{max} = 0.133 v_{a0}/a$. In general, one can use the estimate $\Gamma_{max} \approx 0.1 v_{a0}/a$.

In uniform density (solid and dashed lines in Fig. 2) cases $E_{kin,xy}$ grows exponentially (linear growth phase), reaches maximum amplitude at $t_S \sim 100t_{Au}$ for $a = (1/16)L_z$ and at $t_S \sim 90t_{Au}$ for $a = (1/12)L_z$, and slowly declines in the non-linear regime. The timescale t is in units of the Alfvén crossing time of the characteristic radius a , i.e., $t_{Au} \equiv a/v_{A0}$ where the initial Alfvén velocity on the axis is $v_{A0} \simeq 0.4 c$. The difference in growth is a result of the different wavelengths, longer in case A and shorter in case B. Both cases show similar amplitude of $E_{kin,xy}$ at transition to the non-linear stage. Here we find that the shorter wavelength, $\lambda = 12 a$, grows slightly more rapidly than the longer wavelength, $\lambda = 16 a$, as would be expected if $\lambda_{max} < 12 a$.

In decreasing density cases (dotted lines and dash-dotted lines in Fig. 2), the initial growth in the linear growth phase is more rapid and reaches maximum amplitude at $t_S \sim 50t_{An}$ for $a = (1/16)L_z$ and for $a = (1/12)L_z$, and slowly declines in the non-linear regime. Here the initial Alfvén velocity on the axis is $v_{A0} \simeq 0.3 c$ and it follows that $t_{An} = (4/3)t_{Au}$. This more rapid growth is a result of dependence of the growth rate on the Alfvén velocity. The density decline in the decreasing case leads to a more gradual radial decline in the Alfvén velocity (see Fig. 1g) than for the uniform density cases, and on average a higher Alfvén velocity. The maximum amplitude of $E_{kin,xy}$ relative to the initial volume-averaged magnetic energy for the decreasing density cases is almost the same as the uniform density cases. The maximum radial velocities normalized by the initial axial Alfvén velocity are higher for the decreasing density cases but in absolute terms are almost the same. We note that the normalized maximum radial velocity in the decreasing density cases appears larger than in the uniform density cases because the normalizing axial Alfvén velocity is smaller for the decreasing density cases.

The effect of different radial pitch on the time evolution of $E_{kin,xy}$ and the maximum radial velocity for cases with different radial pitch are shown in Figure 3. The three uniform density and three decreasing density cases show similar linear and non-linear evolution but with different time scales. Growth in the linear stage is more rapid for the decreasing density cases than for the uniform density cases. This can be attributed to the higher average Alfvén velocity in the decreasing density case. For both uniform and decreasing density cases the increasing pitch case ($\alpha = 0.75$) grows more slowly and reaches maximum at a later time with a smaller value for $E_{kin,xy}$ than the constant pitch case ($\alpha = 1.0$). On the other hand, the decreasing pitch case ($\alpha = 2.0$) grows more rapidly and reaches maximum at an earlier time with a larger value for $E_{kin,xy}$ than the

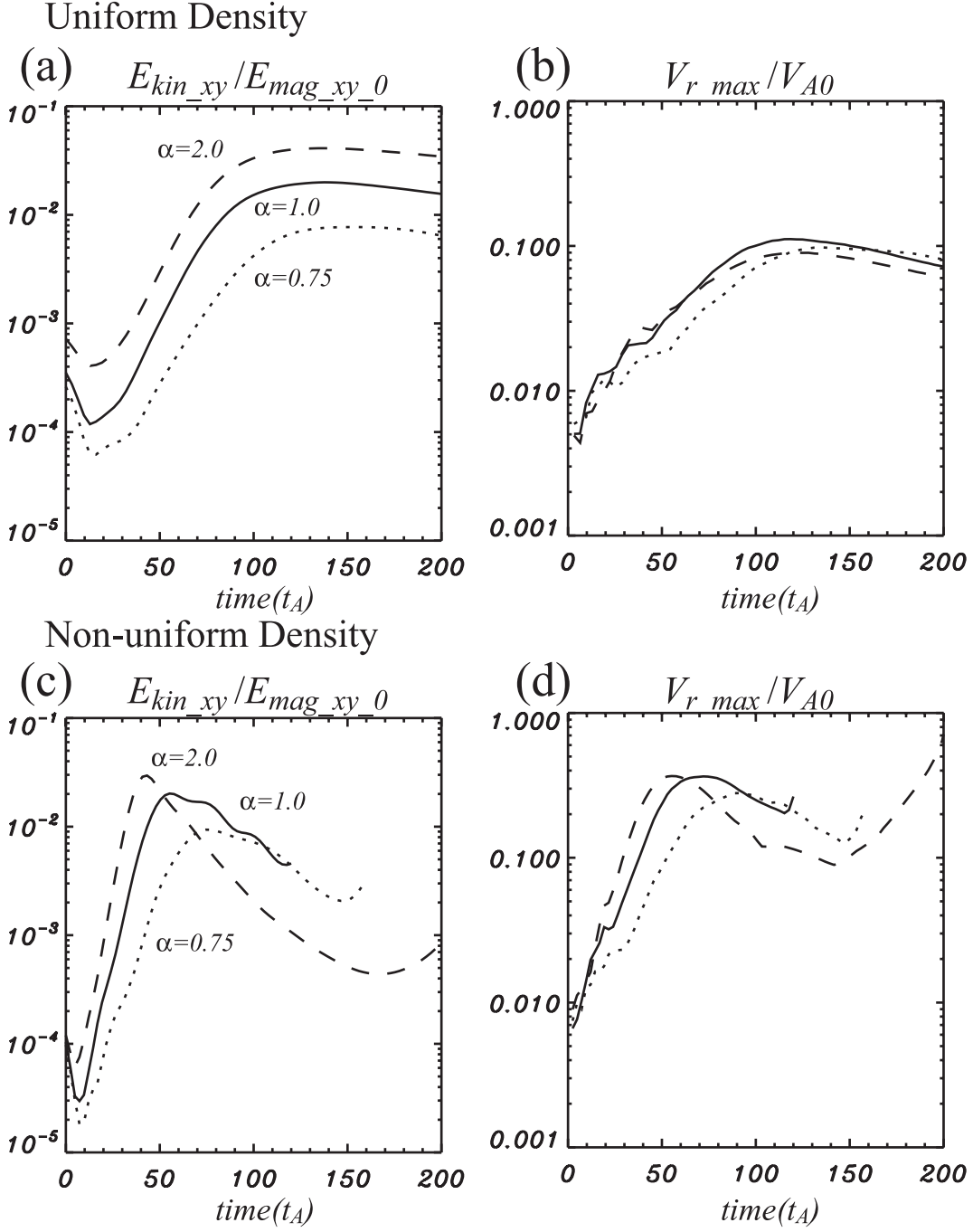


Fig. 3.— Time evolution of (a,c) $E_{kin,xy}$ within $R/L \leq 1.0$ normalized by the initial volume-averaged magnetic energy and (b,d) maximum radial velocity normalized by the initial Alfvén velocity on the axis (v_{A0}). Upper panels show the uniform and lower panels show the decreasing (lower) density cases with constant pitch $\alpha = 1.0$ (solid lines), increasing pitch $\alpha = 0.75$ (dotted lines), and decreasing pitch $\alpha = 2.0$ (dashed lines) cases for $a = (1/8)L$. Time is in units of a/v_{A0} , where v_{A0} is initial Alfvén velocity on the axis. Note that normalizing values of $E_{mag,xy,0}$, V_{A0} and the timescale units, t_A , are different for uniform and decreasing density cases.

constant pitch case. Although the transition time from linear to non-linear evolution is different for each pitch case, the maximum radial velocity is almost the same at transition. The different growth rates as a function of the radial pitch profile are consistent with the non-relativistic linear analysis in Appl et al. (2000).

3.2. Three dimensional structure of the CD kink instability

The results of the previous subsection show that the instability excites relatively slow motions, $v \ll v_A$, and that the overall energy of the system does not vary too much. Nevertheless, the three-dimensional structure of the system is strongly distorted, as will be shown in this subsection. We note that results for case B with the shorter wavelength are essentially the same as for case A. Moreover, the evolution is similar in the uniform and decreasing density cases and only occurs faster in the decreasing density cases. Therefore we show the results of case A with decreasing density only.

Figure 4 shows the time evolution of a density isosurface for the constant pitch case A1n. Displacement of the initial force-free helical magnetic field leads to a helically twisted magnetic filament around the density isosurface. At longer times, the radial displacement of the high density region, best seen in transverse density slices at the grid midplane $z = L_z/2$ (see right panels in Fig. 4), slows significantly. Continuing outwards radial motion is confined to a lower density sheath around the high density core.

The transverse growth of helical twisting is illustrated by the time evolution of magnetic field line displacement seen from the pole-on view shown in Figure 5. Here we follow field lines anchored initially at $R/L = 0.2$ at the $z = 0$ surface. Displacement of the magnetic field rapidly increases with time in the linear stage and the displacement continues to gradually increase throughout the non-linear phase. Thus, the magnetic field displacement indicates continued growth even though the high density region has ceased significant outwards motion by the terminal simulation time. Evolution of the helical perturbation in the magnetic field is accompanied by an appropriate evolution of the current distribution. Initially a large axial current is located near the axis. In the linear growth phase, the axial current is displaced and twists helically. The axial current twist is cospatial with the high density twist. In the linear growth phase the axial current gradually decreases and in the non-linear phase remains constant in magnitude.

Figure 6 shows density isosurfaces and transverse density slices at the grid midplane, $z = L_z/2$, for the cases A2n (increasing pitch) and A3n (decreasing pitch) that can be compared to Figure 4 for case A1n with constant pitch. The 3D density structure from A2n looks similar to that from A1n. The CD kink instability grows exponentially initially. The transverse density slice at the grid midplane (Fig. 6c) shows little outwards motion of the high density region in the non-linear stage similar to the constant pitch case A1n, however, there is little outwards motion in the low density sheath surrounding the high density region. This result is somewhat different from the constant pitch case A1n and suggests a significant reduction in kink amplitude growth. Results from the decreasing pitch case A3n are very different. Figure 6b shows a more slender helical density structure wrapped by the magnetic field. Recall that transition from linear to non-linear evolution was reached at a much earlier time, $t_S \sim 50t_{An}$ (see Fig. 3), than is shown here. While the density cross section (Fig. 6d) is similar to that of the constant pitch case A1n (Fig. 4f), radial motion continues in the non-linear stage to the end of the simulation.

Case: A1n (Non-uniform Density, Constant Pitch, $a=1/8L$), density

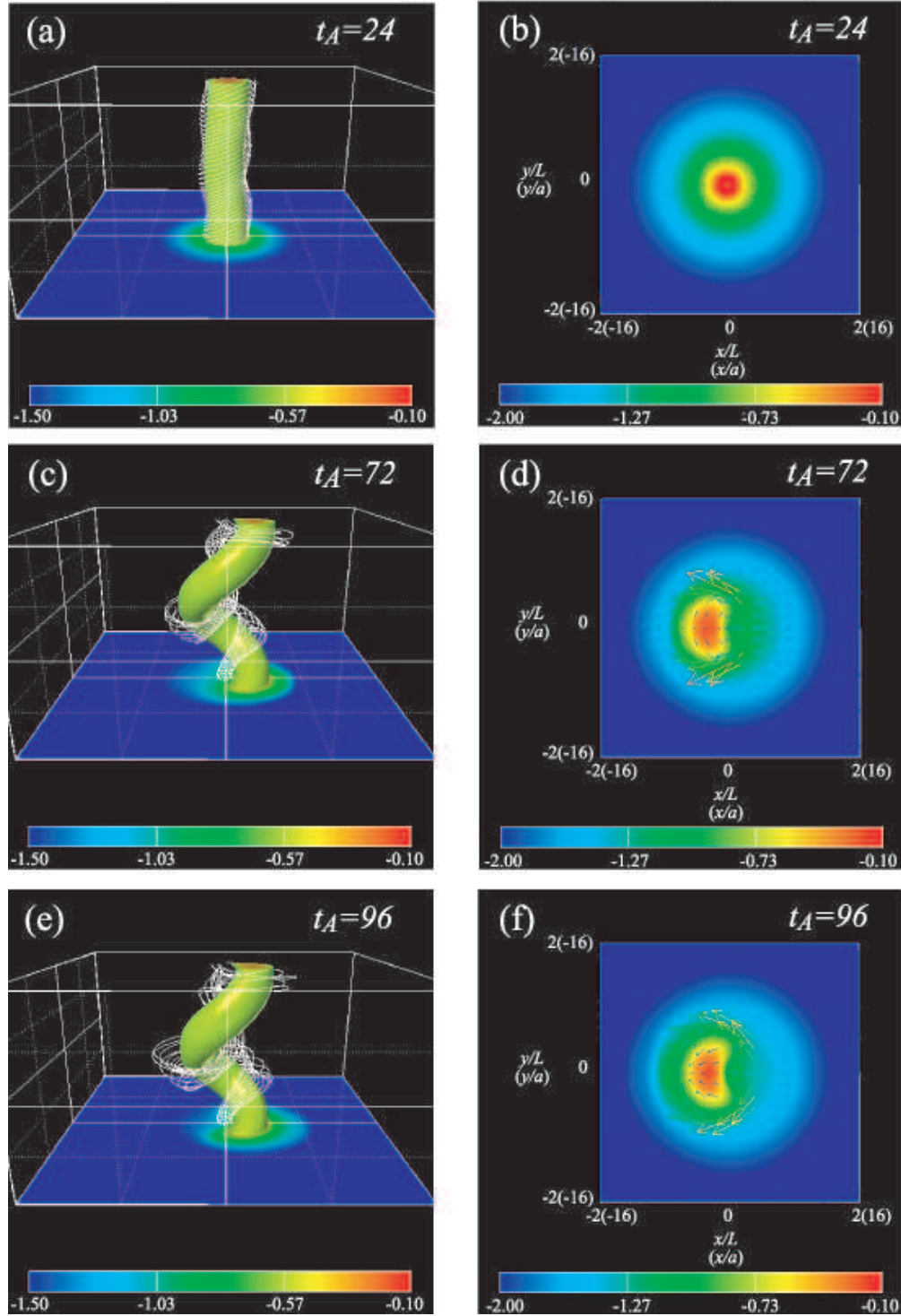


Fig. 4.— 3D density isosurface with transverse slices at $z = 0$ (left) and 2D transverse slices at the grid midplane $z = L_z/2$ (right) for case A1n. Colors show the logarithm of the density with magnetic field (white) lines.

Case: A1n (Non-uniform Density, Constant Pitch, $a=1/8L$)
field lines

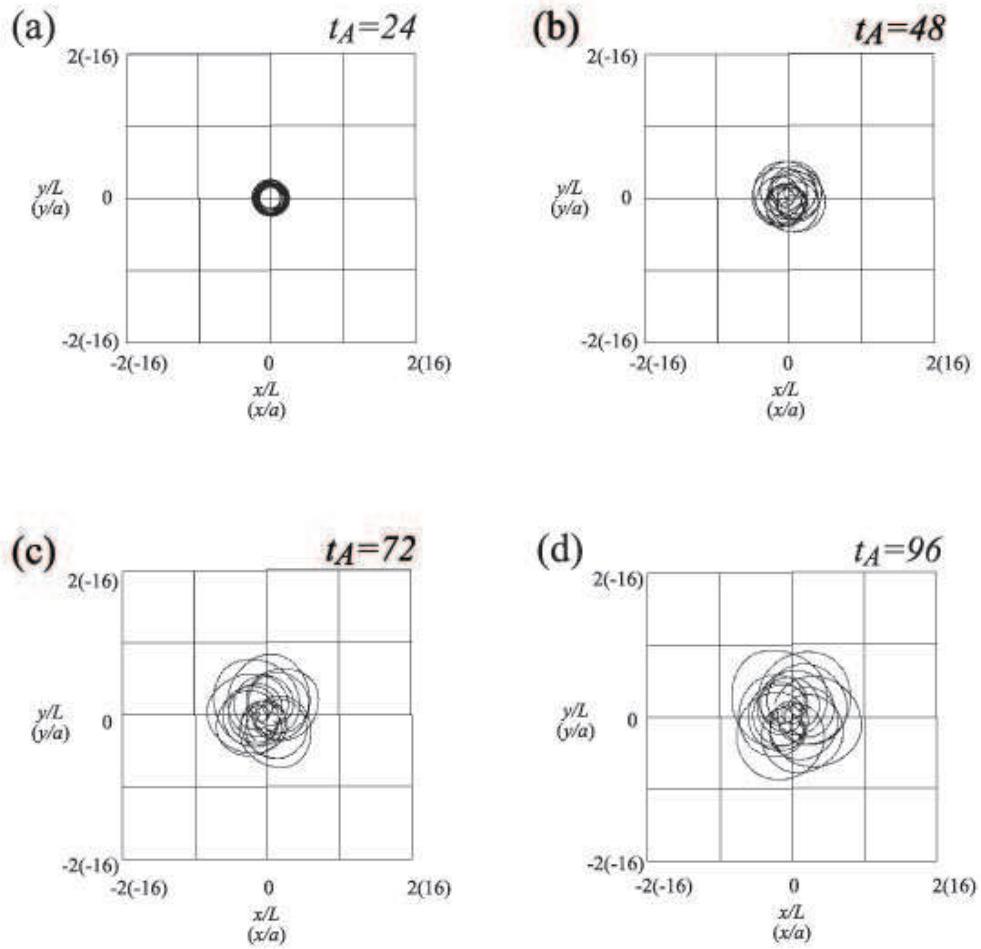


Fig. 5.— Magnetic field structure seen from a pole on view for case A1n.

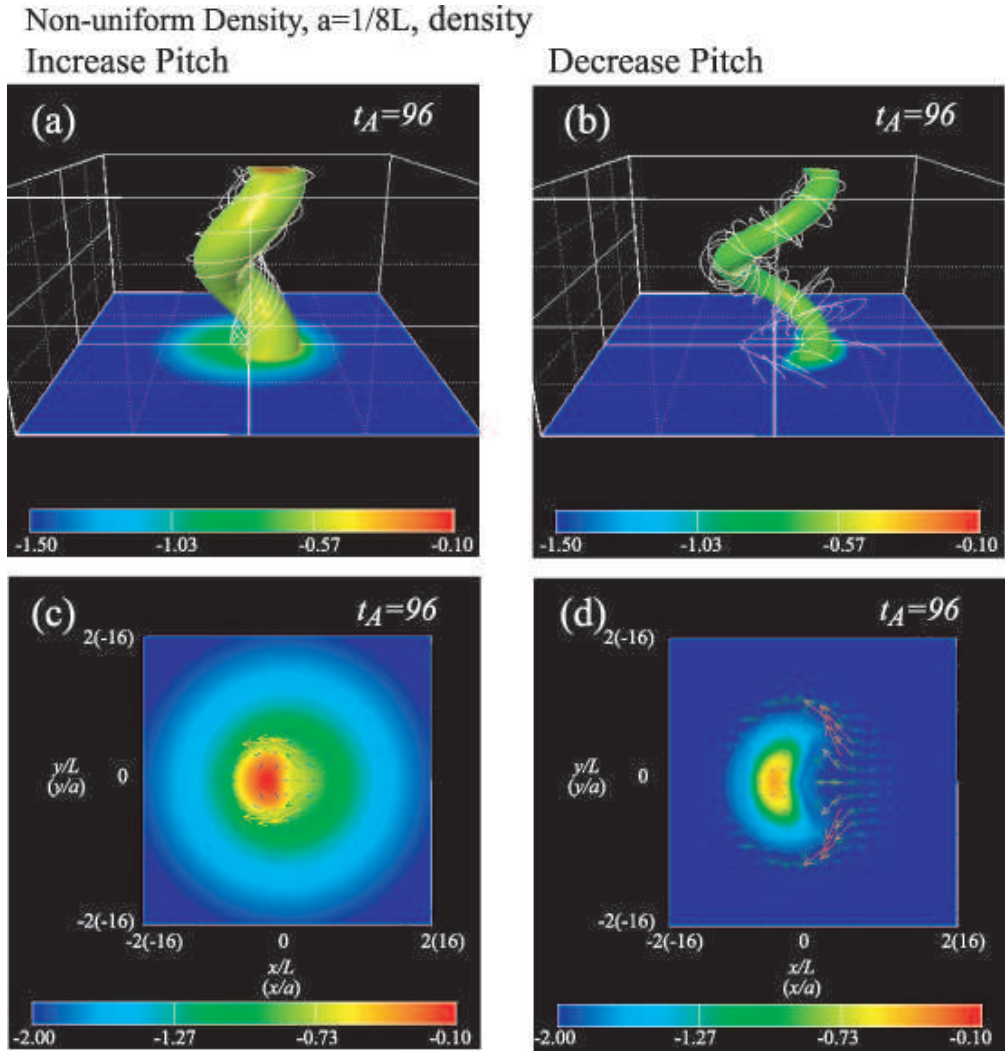


Fig. 6.— 3D density isosurface with transverse slices at $z = 0$ (upper panels) and 2D transverse slices at the grid midplane $z = L_z/2$ (lower panels) for case A2n (left) and A3n (right). Colors show the logarithm of the density with magnetic field (white) lines.

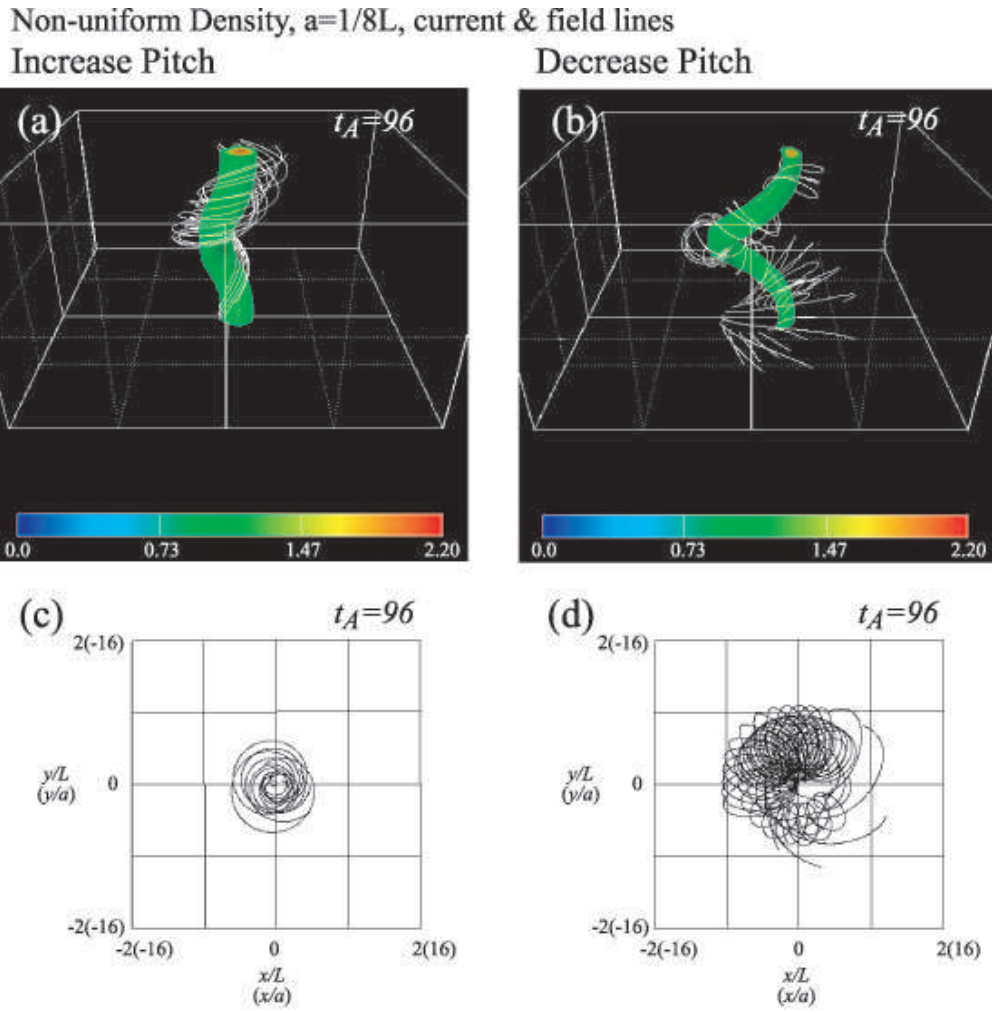


Fig. 7.— 3D axial current, j_z , isosurface (upper panels) with magnetic field (white) lines and (bottom panels) magnetic field structure seen from a pole on view for cases A2n (left) and A3n (right).

Figure 7 shows the axial current isosurface and the magnetic field line displacement seen from the pole-on view for cases A2n and A3n. Like the constant pitch decreasing density case A1n, the axial current twist is cospatial with the high density twist. In the non-linear stage, the helically twisted axial current does not change significantly in case A2n. A pole on view of field lines anchored initially at $R/L = 0.2$ at the $z = 0$ surface (see Fig. 7c) shows that the magnetic field displacement does not increase significantly in the non-linear stage. This along with the density results shown in Figure 6a & c suggest significant non-linear stabilization of the kink mode in the presence of increasing pitch. On the other hand, the axial current isosurface for the decreasing pitch case A3n seen in Figure 7b makes a slender helical structure coincident with the high density structure. Large displacement in the magnetic field can be seen in the pole on view (Fig. 7d).

4. Summary and Discussion

We have investigated development of the CD kink instability of force-free helical magnetic equilibria in order to study the influence of the initial configuration on the linear and nonlinear evolution. We followed the time evolution where the plasma column was perturbed to excite the $m = \pm 1$ azimuthal mode. The kink developed initially as predicted by linear stability analysis. The rate at which the kink developed and, in particular, the non-linear behavior depended on the density and magnetic pitch radial profile. For a constant magnetic pitch profile a density decline with radius led to faster linear growth and made a transition to the non-linear stage sooner than occurred for a uniform density as a result of the more gradual decrease in the Alfvén velocity with radius. While there were some differences in the kink density structure in these two different cases, amplitude growth of the kink continued to the terminal simulation time in both cases.

More profound differences in development accompanied different magnetic pitch profiles. An increase in the magnetic pitch with radius led to a reduced growth rate in the linear (exponential) growth stage and made a transition to non-linear behavior at a later time when compared to the cases with constant magnetic pitch. In the nonlinear stage, amplitude growth of the kink appeared to have ceased by the terminal simulation time. On the other hand, a decrease in the magnetic pitch led to more rapid growth in the the linear growth stage and made a transition to non-linear behavior at an earlier time when compared to the cases with constant magnetic pitch. In the non-linear stage, a slender helical density and current carrying plasma column wrapped by magnetic field developed and amplitude growth continued to increase throughout the simulation. Thus, the linear growth and nonlinear evolution of the CD kink instability depended on the radial density profile and strongly depended on the magnetic pitch profile. Increasing magnetic pitch with radius was clearly stabilizing.

In all cases, the initial axisymmetric structure is strongly distorted by the kink instability, even though not disrupted. It is important to note that the instability develops relatively slowly, that is, the characteristic time for the instability to affect strongly the initial structure is roughly $\tau \sim 100 v_A/a$. The growth rate of the kink instability is roughly $\kappa \sim 0.1 v_A/c$, the exact coefficient

being dependent on the structure of the undisturbed state. Therefore it is not accidental that the full development of the instability takes a long time. In a jet context, our simulations correspond to a perturbation that remains at rest in the flow frame. Therefore, in order to check whether the instability would affect a jet flow, one has to compare τ with the propagation time. In the relativistically moving case, time dilation slows the instability further by the jet Lorentz factor so that the condition for the instability to affect the jet structure may be written as

$$\frac{z}{c\gamma} > 100 \frac{a}{v_A}. \quad (7)$$

In relativistic jets, one could take $v_A \approx c$. In order to find the final criterion, one has to know how the jet radius, a , and Lorentz factor, γ , vary with the distance, z . If the jet is narrow enough so that $\Omega a^2/c < z$, where Ω is the angular velocity at the base of the jet, one can use the scaling (Tschekhovskoy et al. 2008; Komissarov et al. 2009; Lyubarsky 2009) $\gamma \sim \Omega a$. In this case one finds that the criterion for the kink instability is

$$zc > 100\Omega a^2. \quad (8)$$

This means that the instability could affect the jet structure only if the jet expands slowly enough. Assuming the parabolic shape for the jet, $\Omega a/c = \xi(\Omega z/c)^k$, where $k < 1$ and $\xi \sim 1$ are dimensionless numbers, one finds that the instability develops only if $k < 1/2$. Even in this case, the characteristic scale for the development of the instability is very large,

$$\Omega z/c \sim (10\xi)^{2/(1-2k)}. \quad (9)$$

The above estimates should be considered as preliminary because we assumed that the jet moves as a whole so that there is a frame of reference in which the plasma is at rest. Clearly, the criterion for the CD kink instability can be modified by the effects of relativistic rotation, gradual shear, a surrounding sheath, and sideways expansion. For example, in relativistic Poynting dominated jets the growth rate of the instability strongly depends on the transverse profile of the poloidal magnetic field so that τ goes to infinity when the poloidal field is uniform (Istomin & Pariev 1994, 1996; Lyubarskii 1999). On the other hand, Poynting dominated jets are accelerated such that the acceleration zone spans a large range of scales (Tschekhovskoy et al. 2008; Komissarov et al. 2008; Lyubarsky 2009). Therefore, a small kink growth rate does not necessarily preclude significant growth of helical perturbations. We plan to perform 3D RMHD simulations including some of the missing physical effects such as jet flow and rotation in future work. In particular, this will allow us to investigate the interaction between CD and KH driven structure in the relativistic regime.

Y.M., K.I.N., and P.H. acknowledge partial support by NSF AST-0506719, AST-0506666, NASA NNG05GK73G, NNX07AJ88G, and NNX08AG83G. This work is supported in part by US-Israeli Binational Science Foundation grant 2006170. The simulations were performed on the Columbia Supercomputer at NAS Division at NASA Ames Research Center and the Altix3700 BX2 at YITP in Kyoto University.

A. Numerical Tests

In the simulations presented here numerical viscosity and resistivity are associated with the finite grid resolution. It is generally expected that numerical viscosity affects the quantitative growth or damping of instabilities and numerical resistivity allows unexpected magnetic reconnection even when we assume the ideal MHD condition. Therefore we perform several numerical tests to check whether saturation is adequately captured and investigate how the results in the non-linear evolution stage depend on numerical resolution.

Case: A1u (Uniform density Constant pitch, $a=1/8L$)

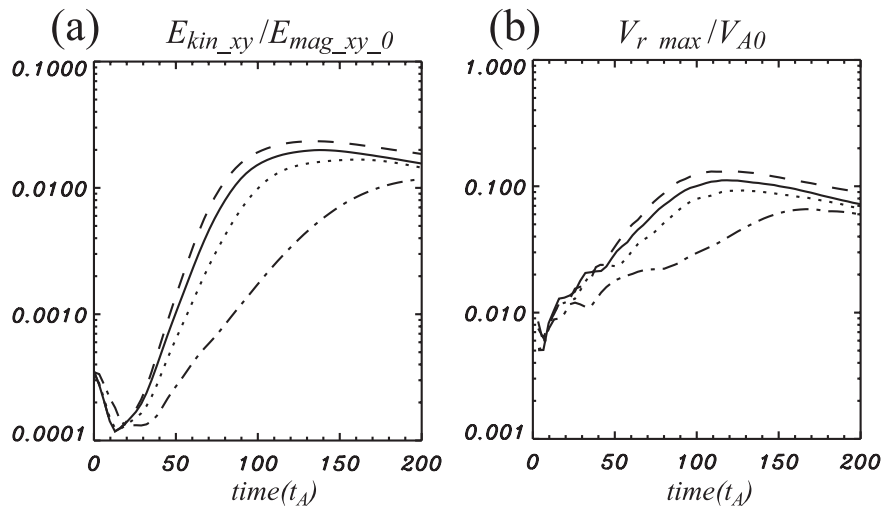


Fig. 8.— Time evolution of (a) $E_{kin,xy}$ normalized by initial volume-averaged magnetic energy within $R/L \leq 1.0$ and (b) maximum radial velocity normalized by initial Alfvén velocity on the axis for case A1u with grid resolution of $\Delta L = L/60$ (dashed), $L/40$ (solid), $L/30$ (dotted), and $L/20$ (dash-dotted).

First, we repeat case A1u (uniform density with constant pitch) for four grid resolutions from 20 to 60 computational zones per simulation length unit $L = 8a$. Figure 8 shows the time evolution of $E_{kin,xy}$ and the maximum radial velocity for different grid resolutions. The results depend on grid resolution. Higher grid resolution shows faster growth and an earlier transition time to the non-linear stage at a larger amplitude. This result is the same as that found in the resolution study of Baty & Keppens (2002). The lowest grid resolution with $\Delta L = L/20$ is clearly inadequate. Although growth does depend on grid resolution, the difference between our choice of $\Delta L = L/40$ and the highest grid resolution of $\Delta L = L/60$ is not significant. Therefore our simulation results adequately capture the CD kink instability.

Second, we check the influence of the transverse boundary. Figure 9 shows the time evolution of $E_{kin,xy}$ and the maximum radial velocity within a box of length $L_z/2$ for a simulation box with transverse boundaries at $x = y = \pm 2L$ ($\pm 16a$) and a simulation box with transverse boundaries

Case: A1u (Uniform density Constant pitch, $a=1/8L$)

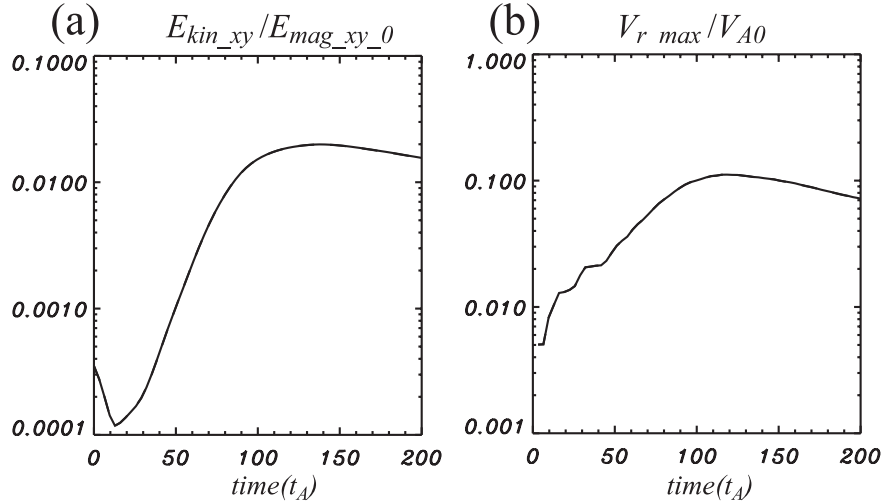


Fig. 9.— Time evolution of (a) $E_{kin,xy}$ normalized by initial volume-averaged magnetic energy within $R/L \leq 1.0$ and (b) maximum radial velocity normalized by initial Alfvén velocity on the axis for case A1u with transverse boundaries at $x = y = \pm 2L$ ($\pm 16a$: solid) and $x = y = \pm 3L$ ($\pm 24a$: dashed).

at $x = y = \pm 3L$ ($\pm 24a$). The results for the time evolution of $E_{kin,xy}$ and the maximum radial velocity are the same in both cases. We conclude that behavior of the CD kink instability is not affected by our choice for the transverse boundary.

Third, we check the influence of the initial gas pressure. In the force-free model we ignore the inertia and pressure of the plasma. However, in the simulation the relativistic ideal MHD equations are solved numerically not the force-free equations. Figure 10 shows the time evolution of $E_{kin,xy}$ and the maximum radial velocity in a box of length $L_z/2$ for an initial pressure of $p_0 = 0.02\rho_0 c^2$ and $p_0 = 0.005\rho_0 c^2$. The results of the time evolution of $E_{kin,xy}$ and the maximum radial velocity show the same linear growth rate in both cases. However, the lower initial pressure case reaches saturation at a slightly later time with higher amplitude but with a larger decline in the non-linear stage. Thus, our required non-zero initial gas pressure does affect the saturation level and non-linear development of the CD kink instability somewhat.

REFERENCES

- Appl, S., Lery, T., & Baty, H. 2000, A&A, 355, 818
- Barkov, M.V. & Komissarov, S.S. 2008, MNRAS, 385, L28
- Bateman, G. 1978, MHD instabilites (Cambridge, Mass., MIT Press, 1978, p.270)

Case: A1n (Non-Uniform density, Constant Pitch, $a=1/8L$)

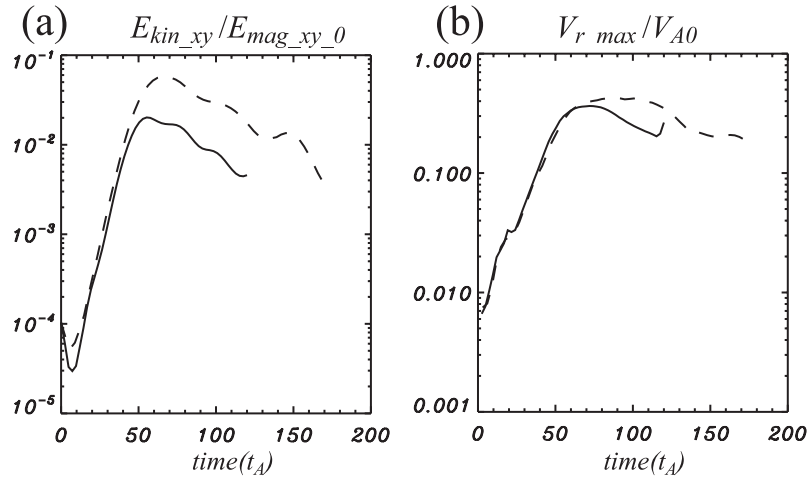


Fig. 10.— Time evolution of (a) $E_{kin,xy}$ normalized by the initial volume-averaged magnetic energy within $R/L \leq 1.0$ and (b) the maximum radial velocity normalized by the initial axial Alfvén velocity on the axis for case A1n with an initial pressure of $p_0 = 0.02\rho_0c^2$ (solid) and with a lower initial pressure of $p_0 = 0.005\rho_0c^2$ (dashed).

Baty, H. 2005, A&A, 430, 9

Baty, H. & Keppens, R. 2002, ApJ, 580, 800

Beckwith, K., Hawley, J.F., & Krolik, J.H. 2008, ApJ, 678, 1180

Begelman, M.C. 1998, ApJ, 493, 291

Begelman, M. C., Blandford, R.D., & Rees, M.J. 1980, Nature, 287, 307

Blandford, R.D. 1976, MNRAS, 176, 465

Blandford, R.D. & Payne, D.G. 1982, MNRAS, 199, 883

Blandford, R. D. & Znajek, R.L. 1977, MNRAS, 179, 433

Bromberg, O. & Levinson, A. 2008, preprint (arXiv:0810.0562)

Carey, C.S. & Sovinec, C.R. 2009, preprint (arXiv:0902.0369)

De Villiers, J.-P., Hawley, J.F., & Krolik, J.H. 2003, ApJ, 599, 1238

De Villiers, J.-P., Hawley, J.F., Krolik, J.H., & Hirose, S. 2005, ApJ, 620, 878

Ferrari, A. 1998, ARA&A, 36, 539

Fukue, J. 1990, PASJ, 42, 793

- Georganopoulos, M. & Kazanas, D. 2003, *ApJ*, 594, L27
- Ghisellini, G., Tavecchio, F., & Chiaberge, M. 2005, *A&A*, 432, 401
- Giannios, D., Uzdensky, D.A., & Begelman, M.C. 2009, *MNRAS*, accepted (arXiv:0901.1877)
- Gómez, J.-L., Marscher, A.P., Antonio, A., Jorstad, S.G., & Agudo, I. 2001, *ApJ*, 561, L161
- Hardee, P.E. 2004, *Ap&SS*, 293, 117
- Hardee, P.E. 2007, *ApJ*, 664, 26
- Hardee, P., Mizuno, Y., & Nishikawa, K.-I. 2007, *Ap&SS*, 311, 283
- Hawley, J.F. & Krolik, J.H. 2006, *ApJ*, 641, 103
- Istomin, Y. N. & Pariev, V.I. 1994, *MNRAS*, 267, 629
- Istomin, Y.N. & Pariev, V.I. 1996, *MNRAS*, 281, 1
- Koide, S. 2003, *Phys. Rev. D*, 67, 104010
- Komissarov, S.S. 2005, *MNRAS*, 359, 801
- Komissarov, S.S., & Barkov, M. V. 2009, *MNRAS*, submitted (arXiv:0902.2881)
- Komissarov, S.S., & McKinney, L.C. 2007, *MNRAS*, 377, L49
- Komissarov, S.S., Barkov, M.V., Vlahakis, N., & Königl, A. 2007, *MNRAS*, 380, 51
- Komissarov, S.S., Vlahakis, N., Königl, A., & Barkov, M.V. 2008, *MNRAS*, submitted (arXiv:0811.1467)
- Königl, A. & Choudhuri, A.R. 1985, *ApJ*, 289, 173
- Lery, T., Baty, H., & Appl, S. 2000, *A&A*, 355, 1201
- Liu, Y.T., Shapiro, S.L., & Stephens, B.C. 2007, *Phys. Rev. D*, 76, 084017
- Lobanov, A.P. & Zensus, J.A. 2001, *Science*, 294, 128
- Lovelace, R.V.E. 1976, *Nature*, 262, 649
- Lyubarskii, Y.E. 1999, *MNRAS*, 308, 1006
- Lyubarsky, Y. 2009, *ApJ*, submitted (arXiv:0902.3357)
- McKinney, J.C. 2005, *ApJ*, 630, L5
- McKinney, J.C. 2006, *MNRAS*, 368, 1561

- McKinney, J.C., & Blandford, R.D., 2008, MNRAS, submitted (arXiv:0812.1060)
- McKinney, J.C., & Gammie, C.F. 2004, ApJ, 977
- McKinney, J.C., & Narayan, R. 2007a, MNRAS, 375, 513
- . 2007b, MNRAS, 375, 531
- Meier, D.L. 2005, Ap&SS, 300, 55
- Meier, D.L. Koide, S., & Uchida, Y. 2001, Science, 291, 84
- Mészáros, P. 2006, Rep.Prog.Phys., 69, 2259
- Mirabel, I.F., & Rodriguez, L.F. 1999, ARA&A, 37, 4
- Mizuno, Y., Yamada, S., Koide, S., & Shibata, K. 2004a, ApJ, 606, 395
- . 2004b, ApJ, 615, 389
- Mizuno, Y., Nishikawa, K.-I., Koide, S., Hardee, P., & Fishman, G. J. 2006, in Proc. VI Microquasar Workshop: Microquasars and Beyond, ed. Tomaso (Trieste: SISSA), 45
- Moll, R., Spruit, H. C., & Obergaulinger, M. 2008, A&A, 492, 621
- Nagataki, S. 2009, ApJ, submitted (arXiv:0902.1908)
- Nakamura, M., & Meier, D.L. 2004, ApJ, 617, 123
- Nakamura, M., Li, H., & Li, S. 2007, ApJ, 656, 721
- Narayan, R., McKinney J.C., & Farmer, A.J. 2007, MNRAS, 375, 548
- Narayan, R., Li, J., & Tchekhovskoy, A. 2009, ApJ, submitted (arXiv:0901.4775)
- Ouyed, R., Clarke, D.A., & Pudritz, R.E. 2003, ApJ, 582, 292
- Penrose, R. 1969, Nuovo Cimento, 1, 252
- Piran, T. 2005, Rev. of Mod. Phys., 76, 1143
- Stephens, B.C., Shapiro, S.L., & Liu, Y.T. 2008, Phys. Rev. D, 77, 044001
- Stern, B.E. & Poutanen, J. 2008, MNRAS, 383, 1695
- Tchekhovskoy, A., McKinney, J.C., & Narayan, R. 2008, MNRAS, 388, 551
- . 2009, ApJ, submitted (arXiv:0901.4776)
- Tomimatsu, A., Matsuoka, T., & Takahashi, M. 2001, Phys. Rev. D, 64, 123003

Urry, C M. & Padovani, P. 1995, PASP, 107, 903

Zhang, B. & Mészáros, P. 2004, Int.J.Mod.Phys., A19, 2385